Ocean-driven thinning enhances iceberg calving and retreat of Antarctic ice shelves

Yan Liu[a,b], John C. Moore[a,b,c,d,1], Xiao Cheng[a,b,1], Rupert M. Gladstone[e,f], Jeremy N. Bassis[g], Hongxing Liu[h], Jiahong Wen[i], and Fengming Hui[a,b]

[a]State Key Laboratory of Remote Sensing Science, College of Global Change and Earth System Science, Beijing Normal University, Beijing 100875, China; [b]Joint Center for Global Change Studies, Beijing 100875, China; [c]Arctic Centre, University of Lapland, 96100 Rovaniemi, Finland; [d]Department of Earth Sciences, Uppsala University, Uppsala 75236, Sweden; [e]Antarctic Climate and Ecosystems Cooperative Research Centre, University of Tasmania, Hobart, Tasmania, Australia; [f]Versuchsanstalt für Wasserbau, Hydrologie und Glaziologie, Eidgenössische Technische Hochschule Zürich, 8093 Zurich, Switzerland; [g]Department of Atmospheric, Oceanic and Space Sciences, University of Michigan, Ann Arbor, MI 48109-2143; [h]Department of Geography, McMicken College of Arts & Sciences, University of Cincinnati, OH 45221-0131; and [i]Department of Geography, Shanghai Normal University, Shanghai 200234, China

Iceberg calving from all Antarctic ice shelves has never been directly measured, despite playing a crucial role in ice sheet mass balance. Rapid changes to iceberg calving naturally arise from the sporadic detachment of large tabular bergs but can also be triggered by climate forcing. Here we provide a direct empirical estimate of mass loss due to iceberg calving and melting from Antarctic ice shelves. We find that between 2005 and 2011, the total mass loss due to iceberg calving of 755 ± 24 gigatonnes per year (Gt/y) is only half the total loss due to basal melt of 1516 ± 106 Gt/y. However, we observe widespread retreat of ice shelves that are currently thinning. Net mass loss due to iceberg calving for these ice shelves (302 ± 27 Gt/y) is comparable in magnitude to net mass loss due to basal melt (312 ± 14 Gt/y). Moreover, we find that iceberg calving from these decaying ice shelves is dominated by frequent calving events, which are distinct from the less frequent detachment of isolated tabular icebergs associated with ice shelves in neutral or positive mass balance regimes. Our results suggest that thinning associated with ocean-driven increased basal melt can trigger increased iceberg calving, implying that iceberg calving may play an overlooked role in the demise of shrinking ice shelves, and is more sensitive to ocean forcing than expected from steady state calving estimates.

iceberg calving | basal melt | mass balance | ice shelf | Antarctica

The majority of Antarctica's mass loss to the ocean occurs through its fringing ice shelves via iceberg calving and basal melt (1–3). Although the mass balance of ice shelves has a negligible direct effect on sea level rise (because the ice shelves float freely), the ice shelves buttress the grounded ice upstream and have been shown to play a major role in stabilizing the discharge of grounded ice to the ocean (4–6). Reduction of buttressing due to increased iceberg calving or basal melt leads to thinning and acceleration of inland glaciers (4–7), and may be driven by regional and global changes in atmospheric and oceanic conditions through ice–ocean and ice–atmosphere interactions (4, 5, 7–11). Catastrophic ice shelf disintegration driven by atmospheric warming has led to abrupt ice shelf retreat in the Antarctic Peninsula (5, 11), which, combined with basal melt induced thinning, has contributed to the 34% increased discharge of grounded ice to the ocean from West Antarctica from 1996 to 2006 (6).

The mass balance of an ice shelf is determined by the difference between mass gained from the flux of ice across the grounding line into the ice shelf, deposition of snow on the surface or marine ice on the bottom of the ice shelf, and mass lost by melting (surface and basal) and iceberg calving. In steady state, the ice shelf has no areal extent change (steady-state calving front) and no thickness change (steady-state ice thickness). It is possible to define a steady-state basal melt (or marine ice accretion) necessary to maintain steady-state ice thickness for given cross-grounding line fluxes, surface mass balance, and calving fluxes (2). Similarly, the steady-state iceberg calving is

defined as the calving flux necessary to maintain a steady-state calving front for a given set of ice thicknesses and velocities along the ice front gate (2, 3). Estimating the mass balance of ice shelves out of steady state, however, requires additional information about the change of ice thickness and the change of areal extent of the ice shelf, which is determined by the advance or retreat of the calving front. Several recent studies have sought to estimate the nonsteady-state mass balance of ice shelves at broad scales (2, 3, 12), but these studies indirectly inferred iceberg calving assuming a steady-state calving front, neglecting the contribution of advance or retreat of the calving front to the mass balance of ice shelves (2, 3). Such "flux gate" calculations are inevitably biased, as they underestimate iceberg calving for retreating ice shelves or overestimate it for advancing ice shelves. This deficiency is problematic not only for estimates of the mass balance of ice shelves but also because current models of iceberg calving provide conflicting predictions about whether increased basal melt will lead to an increase or decrease in iceberg calving (1, 13–15).

Here we avoid the assumption of steady-state calving front by combining traditional estimates of ice shelf mass balance with an annual record of iceberg calving events larger than 1 km^2 from all Antarctic ice shelves exceeding 10 km^2 in area for the period 2005–2011. Our observations show that both iceberg calving (Fig. 1) and ice shelf extent (Fig. 2) change over the observational period, proving that the steady-state calving front assumption is invalid. To estimate mass loss due to iceberg calving, we manually

---

Significance

The floating parts of the Antarctic ice sheet ("ice shelves") help to hold back the flow of the grounded parts, determining the contribution to global sea level rise. Using satellite images, we measured, for the first time, all icebergs larger than 1 km^2 calving from the entire Antarctic coastline, and the state of health of all the ice shelves. Some large ice shelves are growing while many smaller ice shelves are shrinking. We find high rates of iceberg calving from Antarctic ice shelves that are undergoing basal melt-induced thinning, which suggests the fate of ice shelves may be more sensitive to ocean forcing than previously thought.

Fig. 1. Spatial distributions of basal melt and iceberg calving. The area of the red circles denotes mass loss due to iceberg calving of 26 basin systems. The dashed lines divide the ocean around Antarctica into five regions: Weddell Sea (60°W–20°E), Indian Ocean (20°E–90°E), Western Pacific Ocean (90°E–160°E), Ross Sea (160°E–130°W), and Bellingshausen/Amundsen Sea (130°W–60°W). Abbreviations of subbasin systems are described in Dataset S1.

delineated annual cumulative area calved based on Envisat Advanced Synthetic Aperture Radar (ASAR) images from the Augusts of 2005, 2006, 2007, 2008, 2009, 2010, and 2011 with visual interpretation and spatial adjustment, in combination with estimates of the average ice thickness of the calved regions from Ice Cloud and Land Elevation Satellite (ICESat) and IceBridge data (*Materials and Methods* and *SI Materials and Methods*).

In addition to annual mass loss due to iceberg calving, observations of surface features on images and recurrence interval of calving provide additional qualitative information about the style of calving (*SI Discussion*). For example, we observe isolated tabular

bergs that detach along the boundary of isolated preexisting fractures visible in a time series of satellite images (Fig. 3*A*). These events are thought to be part of the natural cycle of advance and retreat of ice shelves and are sufficiently infrequent that observational records spanning many decades would be needed to determine nonsteady-state behavior (13, 16–18). In contrast, we also identify more frequent sequences of smaller-scale calving events (typically much less than 100 km²). These disintegration events are sometimes preceded by the formation of melt ponds on the surface of the ice shelf, suggesting hydrofracture-driven disintegration, as occurred for the Larsen B Ice Shelf (Fig. 3*B*) (5, 8, 19).
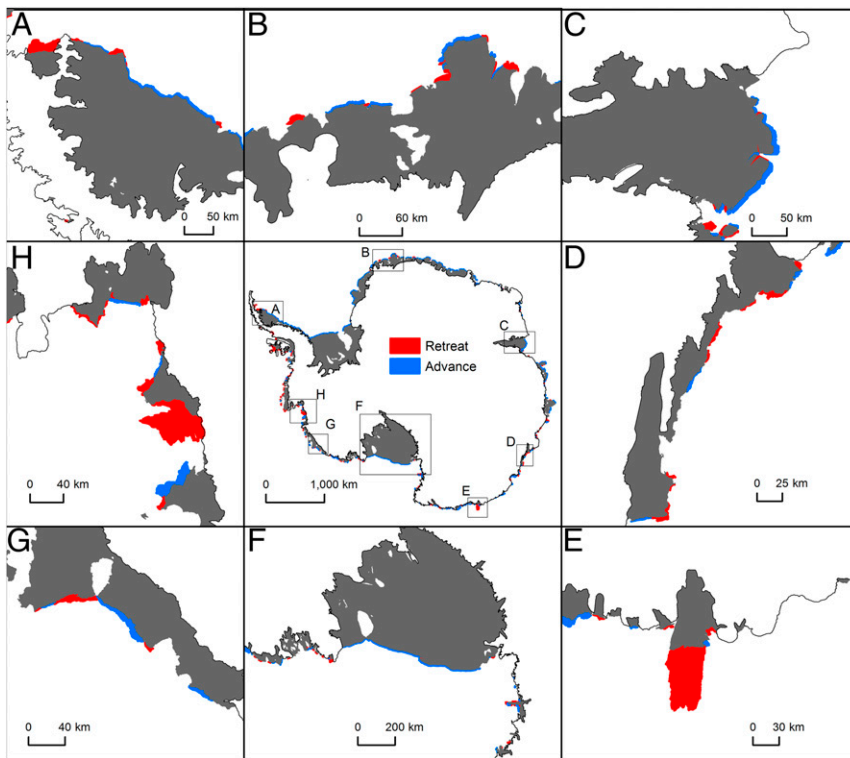
Fig. 2. Antarctic ice shelf advance and retreat between 2005 and 2011. (*A*) Larsen B and C Ice Shelf; (*B*) Fimbulisen, Jelbartisen, and Ekströmisen Ice Shelf; (*C*) Amery Ice Shelf; (*D*) Totten and Moscow University Ice Shelf; (*E*) Mertz Glacier Tongue; (*F*) Ross Ice Shelf; (*G*) Getz Ice Shelf; and (*H*) the floating parts of Pine Island and Thwaites Glaciers, and Crosson Ice Shelf.

Surprisingly, other disintegration events that we observe occurred in colder environments with little or no evidence for surface melt. These events typically occurred in regions with large-scale visible rift and crevasse zones and a rapidly flowing ice front (Fig. 3*C*) and are difficult to detect because the readvance of the ice front partially obscures the change in calving front position.

In conjunction with quantifying iceberg calving, we also developed a flow-line method to quantify cross-grounding line fluxes for the whole of Antarctica (*Materials and Methods*). Using these techniques, we provide an estimate of Antarctic ice shelf mass balance that is not constrained by the steady-state assumption. The mass balance of ice shelves is presented both in terms of volumetric components (net ice shelf volume change

due to thickness and extent changes) and its budget components (surface mass balance, cross-grounding line fluxes, iceberg calving, and basal melt). Moreover, steady-state iceberg calving and steady-state basal melt are also estimated and agree well with previous estimates (2, 3) (Tables S1 and S2). We calculated all these components and associated uncertainties for 7 large drainage systems (Filchner-Ronne, East Antarctica KB, Amery, East Antarctica CE, Ross, West Antarctica, and Peninsula), 26 basin systems labeled A~K', and 94 subbasin systems covering the entire continent (Fig. 1 and Dataset S1).

We find that the mean annual mass balance of all Antarctic ice shelves is slightly positive (46 ± 41 Gt/y) between 2005 and 2011, but with large interannual variability because of the irregular
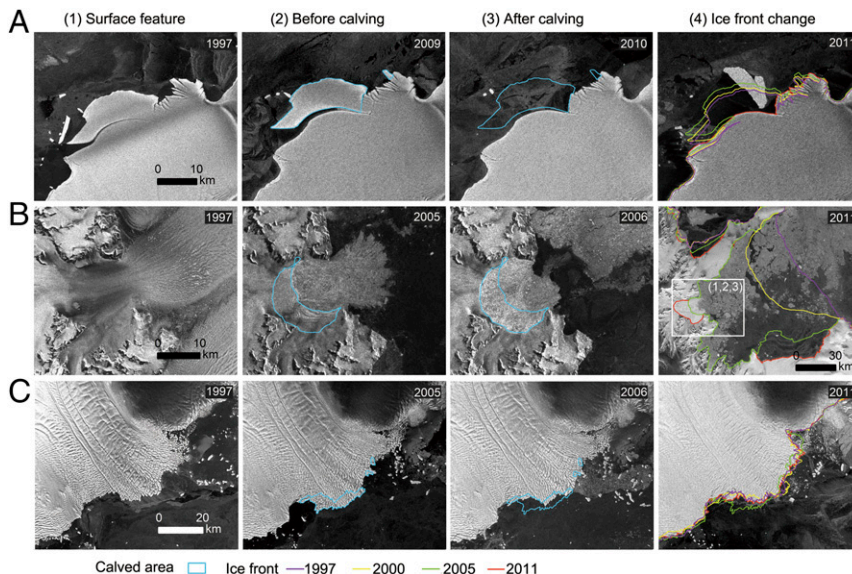

Fig. 3. Different calving features. (*A*) Example of tabular calving from the Fimbulisen Ice Shelf, (*B*) example of melt pond induced disintegration from the Larsen B ice shelf, and (*C*) example of crevasse induced disintegration from the Totten glacier. (*1*) Calving feature on synthetic aperture radar image in 1997 (bright white ponds shown in *B* image are melt ponds). ENVISAT ASAR image with area calved marked before (*2*) and after (*3*) calving. (*4*) Ice front changes overlaid on Envisat ASAR image in 2011.

Table 1. Mean mass balance of Antarctic ice shelves in different state during 2005–2011

Components	State of ice shelf mass balance			
	Negative	Near-zero	Positive	Total
Number of subbasin systems	33	17	43	93*
Total ice shelf area, km^2	284,292	98,522	1,159,293	1,542,108
Ice shelf mass balance, Gt/y	−614 ± 34	4 ± 6	655 ± 37	46 ± 41
Volumetric components, Gt/y				
Mass change due to thickness change	−312 ± 14	−20 ± 5	107 ± 25	−226 ± 25
Mass change due to extent change	−302 ± 27	24 ± 3	549 ± 27	271 ± 21
Budget components, Gt/y				
Grounding line flux	929 ± 60	203 ± 10	838 ± 41	1970 ± 75
Surface mass balance	116 ± 9	30 ± 2	200 ± 9	346 ± 37
Steady-state basal melt	706 ± 92	180 ± 13	405 ± 63	1290 ± 110
Basal melt	1018 ± 90	200 ± 12	298 ± 58	1516 ± 106
Steady-state iceberg calving	339 ± 30	53 ± 4	633 ± 29	1026 ± 39
Iceberg calving	641 ± 24	29 ± 3	84 ± 7	755 ± 25

*One of the 94 subbasin systems has no ice shelf larger than 10 km^2.

occurrence of extralarge-size (larger than 1,000 km^2) calving events (Table 1 and Fig. 4A). Our calculated basal melt of 1516 ± 106 Gt/y accounts for two thirds of Antarctic ice shelf total mass loss while iceberg calving of 755 ± 25 Gt/y accounts for the remaining third (Table 1). The total contribution of iceberg calving to the mass balance might be much higher if the records of infrequent large iceberg detachment are extended by several decades. For example, a sequence of major calving events such as those that detached from the Amery Ice Shelf in 1963–1964 (17) or from the Ross and Filchner-Ronne Ice Shelf in 2001–2002 (20), would result in a (temporary) net negative mass balance for Antarctic ice shelves. We detect 579 distinct iceberg calving events, ranging in size from 1 km^2 to 3,115 km^2 over the 7-y study period. As we have data at monthly resolution for only 3 y (15), the calving events we detect may have resulted from either a sequence of several separate calving events or a single larger calving event. Only three cases larger than 1,000 km^2 are detected: the calving of the Mertz Ice Tongue by iceberg collision (21); the calving of the floating part of Thwaites Glacier by progressive rifting (10); and the disintegration of the Wilkins Ice Shelf, possibly caused by ocean-driven basal melt (19). However, 95% of calving events are small and medium in scale (1~100 km^2 in size), accounting for about 38% of total calving mass over the 7-y study (Tables S3 and S4).

In contrast with recent studies suggesting most ice shelves are close to steady state (3), our basal melt and iceberg calving results (Table 1 and Fig. 4B) indicate significant mass imbalance in more than three quarters of ice shelf subbasin systems. We find two opposing regimes or patterns of mass loss around Antarctica. There are 43 ice shelf subbasin systems in positive mass balance, and, for these ice shelves, basal melt and calving are just 74% ($P < 0.1$ in Student's t test) and 13% ($P < 0.001$), respectively, of their inferred steady-state values (Table 1 and Fig. 4C). Most calving events on these ice shelves produce infrequent, isolated tabular icebergs (Fig. 3A and Fig. S1) and do not reoccur at the same location during our observation period (1997−2011). This previously documented tabular calving style is thought to be primarily controlled by internal stress and characterized by a natural cycle with several decades of quiescence between major calving events (13, 16–18).

There are 33 ice shelf subbasin systems in negative mass balance, but they account for only about 18% of total ice shelf area. These subbasins account for 73% of the total mass loss, comprising 67% of total Antarctic ice shelf basal meltwater production (1018 ± 90 Gt/y) and 85% of total calving (641 ± 43 Gt/y). For these ice shelves, basal melt and calving are 144%

($P < 0.01$) and 189% ($P < 0.01$), respectively, of their steady-state values. Twenty-four of these subbasins experienced both ice shelf retreat and thinning (Dataset S1). We note that the "increased" basal melt we report is referenced relative to our inferred steady-state basal melt and hence, by definition, leads to ice shelf thinning. Similarly, the enhanced iceberg calving is also relative to the steady-state calving required to maintain a constant calving front position and hence "enhanced" calving leads to ice shelf retreat and area loss. Thus, the negative mass balance of these ice shelves results not only from increased basal melt (2, 3, 12) but also from increased iceberg calving. Contributions to the net mass loss from ice shelf thinning and calving front retreat are similar (Table 1). This is true even for the floating parts of Pine Island and Thwaites Glaciers, which are among the best-studied on the continent (22). Both of these ice tongues calved large (larger than 500 km^2) tabular icebergs twice between 1997 and 2011. However, they experienced more frequent sequences of smaller-scale calving events, typically of less than 100 km^2 (Fig. S1 and Table S3). This mode of calving, associated with rapid-flowing ice fronts and intense crevassing and rifting (e.g., Fig. 3C), is common to many of the retreating ice shelves we
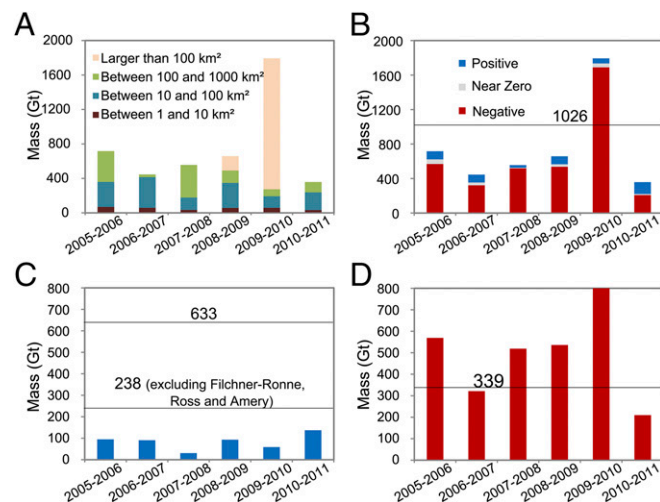

Fig. 4. Annual Antarctic iceberg calving from 2005 to 2011. (A) All ice shelves by calving size; (B) calving by state of mass balance; (C) ice shelves in positive mass balance; and (D) ice shelves in negative mass balance. Horizontal lines in B, C, and D denote steady-state iceberg calving for those ice shelves.

observed. These frequent calving events have been overlooked by previous studies, which assumed that calving is dominated by infrequent tabular berg calving. The calving front retreat associated with ice shelves in negative mass balance has a robustly identifiable trend over our study period (Fig. 4D) due to the shorter recurrence intervals typical of these more frequently calving systems. However, calving (and basal melting) may also vary over decadal and longer time scales not captured by our limited observational period.

The ice shelves undergoing calving front advance and/or ice thickening are the large ice shelf drainage systems (Filchner-Ronne, Ross, and Amery Ice Shelf) together with the neighboring systems of I'J, D'E, and KA', in the Ross Sea, Weddell Sea, and Indian Ocean regions (Fig. 2). These ice shelves account for 78% of the entire Antarctic ice shelf area. They have a positive or near-zero mass balance and are located at high southern latitudes or are fed by an ice sheet grounded well above sea level. These regions are both cold and continental in character and have low net snow accumulation. For some sections of these ice shelves, basal freezing occurs (Fig. 2), which often coincides with observed marine ice "stripes" (23). Marine ice is softer than meteoric ice and has been hypothesized to play an important role in filling and healing bottom crevassing along shear zones, hence determining ice shelf durability (and length of calving cycles) (24–26).

The ice shelves in negative mass balance are primarily small to medium ice shelves located around the Antarctic Peninsula (H'I') and West Antarctica in the Bellingshausen/Amundsen Seas, and East Antarctica along the Wilkes Land coastline (C'D) (Fig. 2, Fig. S1, Dataset S1, and Table S3). The ice shelves in negative mass balance of the Antarctic Peninsula are fed locally, have small grounding line fluxes, and have thinner than average ice fronts (Fig. 2 and Dataset S1). The presence of surface meltwater ponds due to rising atmospheric temperatures has led to catastrophic disintegration events (8, 27), which have only occurred, to date, on the Antarctic Peninsula (24). However, basal melt much larger than necessary to maintain a steady-state ice thickness may have also contributed to the demise of Antarctic Peninsula ice shelves. For example, basal melt exceeded ice flux across the grounding line after 2005 for the more southerly located Wilkins Ice Shelf (Dataset S1), suggesting that it experienced high ocean-driven thinning before disintegration. The southern edge of George VI Ice Shelf is also experiencing increased basal melt and is undergoing similar, but localized, disintegration (7). Increased basal melt driven by warmer water masses beneath the shelves could also diminish or even halt marine ice formation within suture zones that occur in colder ocean environments, reducing the stabilizing effect on basal fractures, and ice shelf structural integrity (25, 26, 28).

The ice shelves in negative mass balance of the West Antarctic systems F'H' and East Antarctic systems CD' are mostly fed by marine based glaciers grounded well below sea level. The rapid response time of these high-throughput systems, which experience high surface accumulation and basal melt (3), may be further increased by the marine ice sheet instability (1) and associated feedbacks. This results in small and potentially vulnerable ice shelves. The presence of both ice shelf thinning and retreat in this region (Dataset S1) hint at a connection between increased basal melt and enhanced iceberg calving. Warm Circumpolar Deep Water (CDW), or slightly modified CDW, lies just off the continental shelf break in these regions (29). Thoma et al. (30) postulated that wind-driven increases in upwelling drive CDW over the continental shelf break and into ice shelf cavities, increasing basal melt and leading to the pronounced observed ice shelf thinning (11, 30, 31). While the relationship between increased basal melt and ocean forcing is clear, it is less clear whether the observed enhanced iceberg calving is simply a direct result of ice shelf thinning or is driven by more complex subshelf processes. It is possible that pronounced and spatially varying basal melt can undercut the submerged ice fronts (9).

Additionally, increased melting of ice mélange, a mixture of sea ice, snow, ice shelf fragments, and marine ice trapped in between the rifts may accelerate rift propagation (32, 33), and threaten ice shelf stability (32, 33). Large-scale crevasse-like surface features are common on the ice shelves along F'H and CD'. Recent observations from ground-penetrating radar show that many of these are, in fact, the surface expression of deep and wide transverse basal crevasses (13, 34) or longitudinal subglacial melt channels (35). The basal channels or crevasses can be incised 200 m into the ice shelf base (34, 35), and the surface depressions can be more than 30 m lower than the usual ice shelf surface (36), making the features the thinnest regions of the ice shelves. These crevasse-like features may provide multiple sites for potential full-thickness crevassing and rift opening. Models show that the tensile stress induced by these wide basal channels is sufficient to cause additional surface and basal crevasse propagation (34, 35). Increased basal melt may enhance this process, as the thinner shelf will flex more and increase the likelihood of full-thickness rift formation (35). For example, Totten Glacier is an ice shelf that has experienced thinning due to increased basal melt, and we observe calving associated with surface troughs (Fig. 3C). These crevasse-like zones cover a considerable area of ice shelves in the F'H' and CD' regions, potentially rendering many Antarctic ice shelves susceptible to massive, catastrophic disintegrations in the event of further increases in basal melt (15).

Given these results, we propose that ocean-driven increased basal melt enhances fracturing of Antarctic ice shelves. We also suggest that the numerous small ice shelves along the Antarctic Peninsula, Amundsen Sea Embayment, and Wilkes Land that have experienced marked increases in basal melt and iceberg calving over the past 2 decades may be poised for major retreat. This needs to be better understood so that it can be factored into future sea level projections.

Materials and Methods

The mass change of an ice shelf, ΔM, over a given time period, Δt, calculated in terms of volumetric components as the sum of change due to mean shelf thickness change, ΔM_H (negative for thinning), and change due to areal extent change (i.e., advance/retreat of ice front), ΔM_A (negative for retreat), is approximately given by a Taylor Series,

$$\Delta M = \Delta M_H + \Delta M_A = A_0 \Delta H \rho_i + H_0 \Delta A \rho_i \qquad [1]$$

where ρ_i is the ice density, A_0 and ΔA are the reference area and change in area, H_0 and ΔH are the reference mean ice thickness and change in mean ice thickness, and we have neglected higher-order terms in the expansion. The reference values are based on the mean values from the 2005–2011 period. We combined the ice shelf area changes of Antarctic ice shelves in 2005–2011 with 2003–2011 ice thickness and 2003–2008 ice shelf thickness changes to estimate the Antarctic ice shelf mass balance. Ice shelf extent changes are identified by coregistered pairs of monthly ASAR data for August 2005 and August 2011. Ice thicknesses are estimated by combining the direct measurements in 2009–2011 from Multichannel Coherent Radar Depth Sounder (MCORDS) by Operation IceBridge mission with the indirect estimates in 2003–2009 from the Geoscience Laser Altimeter System (GLAS) instrument aboard ICESat (SI Materials and Methods). Average ice shelf thickness change for the period 2003–2008 is derived by the procedure in ref. 12 using ICESat-1 GLAS data.

The mass balance can also be expressed in terms of budget components in Gt/y.

$$\frac{\Delta M}{\Delta t} = F_G + SMB - C - B \qquad [2]$$

where F_G is the integrated flux into the ice shelf across the grounding line (calculated using flux gates; see SI Materials and Methods), C is the rate of change of mass due to iceberg calving, SMB is the surface mass balance (the difference between surface accumulation and ablation rate), and B is the rate of change of mass due to basal melt (negative for freeze-on).

Cross-Grounding Line Flux. We use the Interferometric Synthetic Aperture Radar (InSAR) velocities and ice thicknesses at the flux gates to calculate

cross-grounding line flux F_G. Ice thicknesses are estimated by combining MCORDS data and ICESat GLAS data (*SI Materials and Methods*). Flux gates are positioned at the grounding line as determined by a combination of two published data sets. For the most part, the more accurate InSAR grounding line position is used, but where coverage is lacking, the grounding line from imagery and ICESat GLAS is used to achieve complete coverage. Cross-grounding line flux is determined using a flow-line routing algorithm (*SI Materials and Methods*, Figs. S2 and S3). Ice fluxes are estimated by ice flow across each unit of 900-m-width pixel at the grounding line. More than 20,000 flux units around Antarctica are calculated.

Surface Mass Balance. We use the surface mass balance product derived from a firn model UUFIRNMODELv3.1/ANT forced by climate data from RACMOv3.2/ANT27 for the period 2003–2008 (12).

Iceberg Calving. Iceberg calving is the actual rate of ice mass loss due to iceberg calving rather than a "flux gate" calculation (2, 3). It is calculated as the product of the mean ice thickness of the area loss due to calving and area of annual calving losses (*SI Materials and Methods*). The area enclosed between the outer boundary (ice shelf front) and the inner boundary (fracture line) over the annual interval gives the calving area. Calving areas are manually traced from coregistered pairs of consecutive August 2005–2011 Envisat ASAR image mosaics with a spatial resolution of 75 m and geolocation accuracy of 50 m (*SI Data*). Because ice shelves move forward, calving area detection requires tracing both ice shelf margin (ice front) and the fracture line in the original image (before calving) and the second image (after calving). The ice front is delineated by an automated object-oriented classification method based on watershed segmentation combined with manual modifications (Fig. S4 *A* and *B*). Identifying the fracture line is done manually with visual interpretation and spatial adjustment. In the case of tabular calving (Fig. 3*A*), calving area at the ice shelf front is obviously visible; in the case of calving associated with large-scale crevassing (Fig. 3*C*), surface features at the ice front of the second image can be matched with features in the original image, allowing the fracture line to be estimated (Fig. S4 *C* and *D*); in the other case of calving (e.g., Fig. 3*B*) where features cannot be uniquely identified, advance of the starting ice front is estimated by a flow-line method (*SI Materials and Methods*).

Basal Melt. An estimate for B is obtained by rearranging Eq. **2**.

$$B = F_G + SMB - C - \frac{\Delta M}{\Delta t}. \qquad [3]$$

Steady-State Iceberg Calving. The steady-state iceberg calving, assuming no change of ice shelf areal extent, is the sum of iceberg calving and mass change rate due to extent change (positive for advance and negative for retreat).

$$C_{ss} = C + \frac{\Delta M_A}{\Delta t} \qquad [4]$$

Steady-State Basal Melt. The steady-state basal melt, assuming no change of ice shelf thickness, is calculated as the sum of basal melt and mass change rate due to ice thickness change (positive for ice thickening and negative for ice thinning).

$$B_{ss} = B + \frac{\Delta M_H}{\Delta t}. \qquad [5]$$

1. Moore JC, Grinsted A, Zwinger T, Jevrejeva S (2013) Semi-empirical and process-based global sea level projections. *Rev Geophys* 51(3):484–522.
2. Depoorter MA, et al. (2013) Calving fluxes and basal melt rates of Antarctic ice shelves. *Nature* 502(7469):89–92.
3. Rignot E, Jacobs S, Mouginot J, Scheuchl B (2013) Ice-shelf melting around Antarctica. *Science* 341(6143):266–270.
4. Dupont TK, Alley RB (2005) Assessment of the importance of ice-shelf buttressing to ice-sheet flow. *Geophys Res Lett* 32(4):L04503.
5. Pritchard HD, Vaughan DG (2007) Widespread acceleration of tidewater glaciers on the Antarctic Peninsula. *J Geophys Res* 112(F3):F03S29.
6. Rignot E, et al. (2008) Recent Antarctic ice mass loss from radar interferometry and regional climate modelling. *Nat Geosci* 1(2):106–110.
7. Holt TO, Glasser NF, Quincey DJ, Siegfried MR (2013) Speedup and fracturing of George VI Ice Shelf, Antarctic Peninsula. *Cryosphere* 7:797–816.
8. Scambos TA, Hulbe CL, Fahnestock MA (2003) Climate-induced ice shelf disintegration in the Antarctic Peninsula. *Antarct Res Ser* 79:79–92.
9. Rignot E, Koppes M, Velicogna I (2010) Rapid submarine melting of the calving faces of West Greenland glaciers. *Nat Geosci* 3(3):187–191.
10. MacGregor JA, Catania GA, Markowski MS, Andrews AG (2012) Widespread rifting and retreat of ice-shelf margins in the eastern Amundsen Sea Embayment between 1972 and 2011. *J Glaciol* 58(209):458–466.
11. Jacobs SS, Jenkins A, Giulivi CF, Dutrieux P (2011) Stronger ocean circulation and increased melting under Pine Island Glacier ice shelf. *Nat Geosci* 4(8):519–523.
12. Pritchard HD, et al. (2012) Antarctic ice-sheet loss driven by basal melting of ice shelves. *Nature* 484(7395):502–505.
13. Bassis JN, Jacobs SS (2013) Diverse calving patterns linked to glacier geometry. *Nat Geosci* 6(10):833–836.
14. Nick FM, et al. (2013) Future sea-level rise from Greenland's main outlet glaciers in a warming climate. *Nature* 497(7448):235–238.
15. Åström JA, et al. (2014) Termini of calving glaciers as self-organized critical systems. *Nat Geosci* 7:874–878.
16. Joughin I, MacAyeal DR (2005) Calving of large tabular icebergs from ice shelf rift systems. *Geophys Res Lett* 32(2):L02501.
17. Fricker HA, Young NW, Allison I, Coleman R (2002) Iceberg calving from the Amery Ice Shelf, East Antarctica. *Ann Glaciol* 34(1):241–246.
18. Bassis JN, Fricker HA, Coleman R, Minster J-B (2008) An investigation into the forces that drive ice-shelf rift propagation on the Amery Ice Shelf, East Antarctica. *J Glaciol* 54(184):17–27.
19. Scambos TA, et al. (2009) Ice shelf disintegration by plate bending and hydro-fracture: Satellite observations and model results of the 2008 Wilkins ice shelf break-ups. *Earth Planet Sci Lett* 280(1):51–60.
20. Jakobsson M, et al. (2011) Geological record of ice shelf break-up and grounding line retreat, Pine Island Bay, West Antarctica. *Geology* 39(7):691–694.
21. Young NW, Legresy B, Coleman R, Massom R (2010) Mertz Glacier tongue unhinged by giant iceberg. *Aust Antarct Mag* 18:19.
22. Pritchard HD (2014) Bedgap: Where next for Antarctic subglacial mapping? *Antarct Sci* 26(6):742–757.
23. Lambrecht A, Sandhager H, Vaughan DG, Mayer C (2007) New ice thickness maps of Filchner-Ronne Ice Shelf, Antarctica, with specific focus on grounding lines and marine ice. *Antarct Sci* 19(4):521.
24. Scambos TA, Bohlander J, Shuman CA, Skvarca P (2004) Glacier acceleration and thinning after ice shelf collapse in the Larsen B embayment, Antarctica. *Geophys Res Lett* 31(18):L18402.
25. Holland PR, Corr HF, Vaughan DG, Jenkins A, Skvarca P (2009) Marine ice in Larsen ice shelf. *Geophys Res Lett* 36(11):L11604.
26. Kulessa B, Jansen D, Luckman AJ, King EC, Sammonds PR (2014) Marine ice regulates the future stability of a large Antarctic ice shelf. *Nat Commun* 5:3707.
27. MacAyeal DR, Scambos TA, Hulbe CL, Fahnestock MA (2003) Catastrophic ice-shelf break-up by an ice-shelf-fragment-capsize mechanism. *J Glaciol* 49(164):22–36.
28. McGrath D, et al. (2014) The structure and effect of suture zones in the Larsen C Ice Shelf, Antarctica. *J Geophys Res* 119(3):588–602.
29. Weertman J (1973) Can a water-filled crevasse reach the bottom surface of a glacier? *Int Assoc Sci Hydrol Publ* 95:139–145.
30. Thoma M, Jenkins A, Holland DM, Jacobs SS (2008) Modelling circumpolar deep water intrusions on the Amundsen Sea continental shelf, Antarctica. *Geophys Res Lett* 35(18):L18602.
31. Dinniman MS, Klinck JM, Hofmann EE (2012) Sensitivity of Circumpolar Deep Water transport and ice shelf basal melt along the west Antarctic Peninsula to changes in the winds. *J Clim* 25(14):4799–4816.
32. Khazendar A, Rignot E, Larour E (2009) Roles of marine ice, rheology, and fracture in the flow and stability of the Brunt/Stancomb-Wills Ice Shelf. *J Geophys Res* 114(F4):F04007.
33. Larour E, Rignot E, Aubry D (2004) Modelling of rift propagation on Ronne Ice Shelf, Antarctica, and sensitivity to climate change. *Geophys Res Lett* 31(16):L16404.
34. McGrath D, et al. (2012) Basal crevasses and associated surface crevassing on the Larsen C ice shelf, Antarctica, and their role in ice-shelf instability. *Ann Glaciol* 53(60):10–18.
35. Vaughan DG, et al. (2012) Subglacial melt channels and fracture in the floating part of Pine Island Glacier, Antarctica. *J Geophys Res* 117(F3):F03012.
36. Liu Y, et al. (2014) Detection of crevasses over polar ice shelves using Satellite Laser Altimeter. *Sci China Earth Sci* 57(6):1267–1277.

Supporting Information

Liu et al. 10.1073/pnas.1415137112

SI Discussion

Characteristics of Antarctic Iceberg Calving.

Spatial distribution of iceberg calving in different styles. Previous observations of surface features on images have documented two styles of iceberg calving: "tabular" calving (1–4) and "disintegrating" calving (3, 5–7). The infrequent repeat interval of our imagery precludes us from determining if the disintegration events we detect initiated as a single tabular berg that disintegrated after detaching or as a sequence of individual bergs that detached from the calving front along preexisting crevasses. Moreover, because large tabular events detach infrequently, our observations provide little information about whether ice shelves that predominantly experienced disintegration style events during our observation period are more or less prone to tabular berg detachment. Nonetheless, because smaller-scale disintegration events occur frequently, our observations do inform about the absence of disintegration events from ice shelves. Thus, we use recurrence interval (*Iceberg calving*) to classify our observed events into infrequent and frequent calving, which may then indicate tabular or disintegration styles.

Identification of the recurrence of a calving event requires that the recurred event happens in the same spatial neighborhood as the first, and that the two events are of the same order of magnitude. By this definition, only 152 of the 579 calving events did not recur in the period of 1997–2011. Surface features suggest that these events are tabular berg detachment. In this paper, we thus classify them as infrequent "tabular" calving event and classify the other 427 events as frequent "disintegration" calving events.

Fig. S1 and Table S3 show the spatial distribution of the 579 iceberg calving events occurred in Antarctica from 2005 to 2011. Frequent disintegration calving dominates in the Peninsula, West Antarctica, and the East Antarctica CE sectors, which also have the largest number of calving events. For example, Totten Glacier (sector CE) and Wilkins Ice Shelf (Peninsula) calve nearly every year. In contrast, infrequent tabular calving dominates the East Antarctica KB, Ross, and Amery sectors. No calving event was observed in the Filcher-Ronne sector.

Spatial scale features of Antarctic iceberg calving. Mean percentage of calving events, area, and mass loss binned into four different spatial scale categories from 2005 to 2011 are shown in Table S4. Frequency increases as calving area decreases, but there is a relatively small increase at the smallest scales. By contrast, mean annual calving area and mass loss in the medium, large, and extra-large calving scales are similar, and sum to more than 93% of the total. The calving events of less than 100 km^2, which were often ignored in previous studies, accounted for 95% of the mean annual number of events, 32% of the area loss, and 38% of mass loss. However, the smallest size scale (less than 10 km^2) contributes less than 7% of total mass loss. This suggests that observations of smaller calving events will only slightly improve the accuracy of our estimate but add significant workload. Thus, the spatial resolution of ASAR data satisfies the needs for calving area detection (see also *SI Data*).

Characteristics of Antarctic Ice Shelf Mass Balance.
The detailed results of Antarctic ice shelf mass balance and its components are shown in Dataset S1.

Comparison with Other Studies.

Comparison of area delineation. A previous estimate of total area of Antarctic ice shelves is 1,561 million km^2, reflecting ice front location in 2007–2008 (8), whereas our 1,542 million km^2 shows the average over 2005–2011 (Dataset S1).

Comparison of cross-grounding line flux. We use the methods of least-squares estimate (LSE) and York's linear regression with errors (9) to compare our estimated ice flux to previous results (10). This shows that there is good consistency between these two different methods ($R > 0.9$). We expect the two results to be different because earlier work (10) did not include about 20% of the total Antarctic grounding line (GL), while we make use of our flow-line routing algorithm to calculate the whole GL flux.

Comparison of steady-state calving flux. Table S1 shows that our result is slightly lower than found by earlier studies (8). However, the previous methods are susceptible to overestimation of ice front flux gate lengths if the shape of ice shelf margins is complex, especially where the presence of rifts complicates the geometry. Even considering the angle between flow direction and ice front line cannot completely remove the effect of overlapping flux gates.

Comparison of basal melt. Area mean basal melt rates in meters per year from our study, and the glaciological estimate (8), the Finite-Element Sea-Ice Ocean Model (FESOM) model (11), and the Bremerhaven Regional Ice Ocean Simulations (BRIOS) model (12) are compiled in Table S2. Melt rates from this study are consistent with the glaciological estimate (8), except for melt under the Filchner-Ronne Ice Shelf mainly due to the quite different thickening rates of the shelf. We use the same source for ice shelf change rates as ref. 8, but our study shows a mass gain from ice shelf thickening of 73 ± 18 Gt/y, in accordance with the ice shelf thickening rate of 0.02 ± 0.005 m/y (13), while ref. 8 shows mass loss from ice shelf thinning of 61 ± 18 Gt/y. A possible explanation for the difference may be that ref. 8 assumes steady state.

SI Data

We use multisource satellite data, updated remote sensing-based products, and model products to quantitatively estimate geometric and flux components of Antarctic ice shelf mass balance. The key parameters are calculated with data that have low uncertainties and high time consistence. These data include remote sensing images, surface elevation, ice thickness, surface ice flow velocity, GL, ice thickness, geoid model for geoid correction of surface elevation, firn depth correction (FDC) for ice thickness calculation, and land cover map. We also used published data, including surface mass balance and ice thickness change of Antarctic ice shelves.

The data sets used to calculate ice shelf mass balance and its volumetric and budget components in this study can be found at the following websites: bprc.osu.edu/rsl/radarsat/data/ [RAMP AMM-1 SAR Image Mosaic of Antarctica (14)], nsidc.org/data/nsidc-0280 [MODIS Mosaic of Antarctica (MOA) (15)], earth.esa.int [European Space Agency (ESA) Environmental Satellite (Envisat) ASAR Wide-Swath Mode (WSM) image (2005–2011)], nsidc.org/data/docs/daac/glas_icesat_l1_l2_global_altimetry.gd.html [GLAS/ICESat L1 and L2 Global Altimetry Data, Version 33 (16)], nsidc.org/data/irmcr2 [IceBridgeMultichannel Coherent Radar Depth Sounder (MCORDS) L2 Ice Thickness (17)], www.antarctica.ac.uk//bas_research/our_research/az/bedmap2 [Bedmap 2 (18)], nsidc.org/data/docs/measures/nsidc0484_rignot/ [MEaSUREs InSAR-Based Antarctica Ice Velocity Map (19)], nsidc.org/data/docs/measures/nsidc0498_rignot/ [MEaSUREs Antarctic Grounding Line from Differential Satellite Radar Interferometry (DInSAR) (20)], nsidc.org/data/docs/agdc/nsidc0489_bindschadler/ [ASAID High-resolution Image-derived Grounding and Hydrostatic Lines

for the Antarctic Ice Sheet (21)], icgem.gfz-potsdam.de/ICGEM/ [EIGEN-6C2 Geoid (22)], and doi.pangaea.de/10.1594/PANGAEA. 775983 [Surface mass balance (SMB) (13), 2003–2008].

Envisat is an advanced polar-orbiting Earth observation satellite that was launched in March 2002 by ESA. It carries sophisticated optical and radar instruments, and Advanced Synthetic Aperture Radar (ASAR) is the largest single instrument. WSM is one of the five operating modes of ASAR. Envisat ASAR WSM (henceforth simply ASAR) data use the ScanSAR technique with a swath of 405 km and spatial resolution of 150 m, and provides HH (horizontal transmitting, horizontal receiving) and VV (vertical transmitting, vertical receiving) polarization images, and measures radar backscatter strength of C-band 8,000–4,000 MHz (3.8–7.5 cm). Its nominal resolution (pixel size) is 75 m. Generally, it only takes 3 d to cover all Antarctic coastline. ASAR Level 1B product ASA_WSM_1P N1 files are used in this study. Together with precise orbit data from DOR_VOR_AXVF files (available at https://earth.esa.int/), they are geolocated and resampled onto the projected grid based on polar stereographic projection. The geolocation accuracy and precision are tested by a thorough comparison with the RAMP AMM-1 image with an estimated geolocation accuracy of 50 m (23). It showed that the accuracy of geolocation data are better than 75 m (a pixel size). The mosaic ASAR images of August each year in 2005–2011, which repeatedly covered the Antarctic coastline, are used to monitor annual calving events and ice front advance and retreat.

The observations of iceberg calving events of Antarctic ice shelves for the period 2005–2011 are available online at www.nature.com/ngeo/journal/v7/n12/full/ngeo2290.html#supplementary-information (Supplementary Data) and are described in the Calving Event Catalogue (nature.com/ngeo/journal/v7/n12/extref/ngeo2290-s6.pdf).

SI Materials and Methods

Ice Shelf Mass Balance Estimation.

Antarctic surface flow line mapping. The discharge to the Antarctic ice shelves is routed through widespread complex flow in the interior of the Antarctic ice sheet. Surface flow lines (also termed "streamlines") are delineated either by flow directions calculated from Digital Elevation Model (DEM) or by flow features on satellite images usually only distributed in fast flow area that are limited in their potential to track the flow from ice divide to ice shelf front. We propose a method that automatically assesses the starting positions and the whole route of an ice flow line on the surface only based on the horizontal flow direction calculated from the surface velocity map for the period 2007–2008 (*Ice flow velocity*). In a raster map of flow direction, flow direction is the attribute of a grid cell and grid direction is an approximation to ice flow direction, limited by the restriction that flow lines must pass through cell centers. The direction searching accuracy is defined as the difference between flow direction and grid direction. Lookup tables between flow directions and grid directions of different direction searching accuracy are set to adapt to the actual flow direction accuracy of the data, which varies spatially. The highest searching accuracy is up to 0.1 degree. The principle of no crossing between flow lines is used to estimate the actual direction accuracy, which is typically between 0.5 degrees and 5 degrees.

We use this method to track the full range of high-density surface flow lines of Antarctica (Fig. S2), giving the most detailed view of the complex Antarctic flow system to date. The flow lines have a very good agreement with most surface longitudinal features on satellite images. The flow line map shows ice shelf ice origins, flow trajectories and regions of convergence or confluence.

Delineation of Antarctic ice sheet drainage−ice shelf systems. The definition of ice sheet drainage−ice shelf system is an important process when developing estimates both of ice sheet and ice shelf mass balance. A principle aim of this study is to develop estimates of ice shelf mass balance and their relationship with ice

sheet mass balance using common divides. The previous detailed definition of Antarctic ice sheet drainage divides are based on ICESat DEM at 500 m resolution and include 26 distinct basins (10, 24) and 65 drainage subbasins (10) [note that about 1/5 of Antarctic ice is not included within the survey (24)], assigned into three major components of East Antarctica, West Antarctica, and the Peninsula. In contrast, here we include all of the subbasins. We also separate the ice sheet into seven major sectors identified by the routing of ice to major ice shelves (Fig. 1). We delineated drainage divides based on ref. 10, but we added the fringing floating parts delineated by the ice flow-line routing algorithm (Fig. S2).

In this study, Antarctic ice sheet drainage−ice shelf system is divided into 7 sectors, 26 basin systems, and 94 subbasin systems. The seven sectors include the Filcher-Ronne Ice Shelf system (Filchner-Ronne), East Antarctica KB system (East Antarctica KB), Amery Ice Shelf system (Amery), East Antarctica CB system (East Antarctica CE), Ross Ice Shelf system (Ross), West Antarctica F'H system (West Antarctica), and Antarctic Peninsula system (Peninsula) (Fig. S1). Every sector has several basin systems labeled A to K'. Ninety-four individual subsystems are grouped into large units (Fig. 1 and Dataset S1).

Delineation of ice shelf extent. The area between the GL and ice front excluding ice rises and islands is defined as ice shelf extent. All of the ice shelves larger than 10 km² are included in this paper (Dataset S1). Differential Interferometric Synthetic Aperture Radar (DInSAR) derived Antarctic GL in 1994–2009 [one dataset of the NASA Making Earth System Data Records for Use in Research Environments (MEaSUREs), available at nsidc.org/data/docs/measures/nsidc0498_rignot/] (19, 20), complemented with visible imagery in 1999–2003 and laser altimetry in 2003–2009 derived Antarctic GL [one dataset of the Antarctic Surface Accumulation and Ice Discharge (ASAID) project, available at nsidc.org/data/docs/agdc/nsidc0489_bindschadler/) (21), are selected. Ice front coastlines are identified in two mosaics of monthly ASAR data for August 2005 and August 2011, respectively. The thorough comparison with the first Antarctic Mapping Mission (AMM-1) synthetic aperture radar images of the Canadian RADARSAT-1/2 satellites (RADARSAT-1/2 images) and coastlines (14, 25) are used to test the consistency and quality. The ice fronts delineated from ASAR data have a good agreement with RADARSAT-1/2 ice front in ice front areas with little or no change. Averages of ice shelf area in 2005 and 2011 are used in estimation of volume ice shelf thickening or thinning (*Ice shelf thickening or thinning*) and area mean basal melt rates (*Basal melt*).

Ice thicknesses. We calculate thicknesses at GLs and ice shelf fronts for estimating GL fluxes, iceberg calving rates, and mass gain (or loss) from advance (or retreat). Ice thickness is calculated using direct measurements of actual thickness from the NASA IceBridge Mission (IceBridge) MCORDS and indirect estimates from ICESat Geoscience Laser Altimeter System (GLAS) derived ice shelf surface elevation assuming hydrostatic equilibrium. The data are available at the National Snow and Ice Data Center (NSIDC) (nsidc.org/data/icebridge/data_summaries.html and nsidc.org/data/icesat/data.html). Ice thicknesses from Bedmap2 (18) are used for no-data areas and consideration of marine ice under ice shelves (available at antarctica.ac.uk//bas_research/data/access/bedmap/).

Individual thickness calculation. The actual thickness of an ice shelf H includes one, two, or three layers, i.e., firn, meteoric ice, and marine ice layers. Generally, meteoric and marine ice layers are lumped together as a single layer. Thus,

$$H = h_f + h_i, \qquad \text{[S1]}$$

where h_i is the total thickness of meteoric ice layer and marine ice layer and h_f is the firn thickness.

Although the actual thickness of the ice shelf is an important geometry parameter, ice equivalent thickness, H_i, is used more

often in mass calculations. The ice equivalent thickness refers to the thickness of an ice shelf if all of the ice is at an average ice density ρ_i (917 kg/m^3), i.e., the reduced total thickness obtained by compressing the variable-density firn layer until its density equals that of ice,

$$H_i = (h_f - \Delta h) + h_i, \qquad \text{[S2]}$$

$$h_f \rho_f = (h_f - \Delta h)\rho_i, \qquad \text{[S3]}$$

where ρ_f is average density of the firn layer, and Δh is the FDC, defined as the difference between the combined ice/firn column and the ice equivalent thickness.

MCORDS thickness data have no firn correction (26), so the ice equivalent thickness can be determined by removing an FDC from the MCORDS thickness.

$$H_i = (h_f - \Delta h) + h_i = (h_f + h_i) - \Delta h = H - \Delta h. \qquad \text{[S4]}$$

The ice equivalent thickness can be inferred from surface elevation using the principle of hydrostatic equilibrium.

$$H_i = \frac{(h_{asl} - \Delta h)\rho_w}{\rho_w - \rho_i}, \qquad \text{[S5]}$$

where h_{asl} is ice shelf freeboard, i.e., the height difference between ice shelf surface height and sea surface height, and ρ_w is the density of the seawater column under the ice shelf. Seawater density will vary with depth, so we want a representative density at depths between the ice front (average 220 m) and the GL (average 710 m). Hence, we use 1,027 kg/m^3 with an uncertainty of 5 kg/m^3 as suggested by ref. 27.

We use ICESat GLAS data to obtain the ice shelf freeboard. GLAS data preprocessing in ref. 13 is used in this study. The elevation measured by satellite radar altimeter is referenced to the WGS84 ellipsoid and should be first transformed to the elevation relative to geoid. The local ocean surface is different from global mean sea level resulting from nontidal effects. The mean dynamic topography (MDT) is defined as the height of the mean ocean surface relative to the geoid. Ice shelf freeboard is calculated as

$$h_{asl} = ele - geoid - MDT, \qquad \text{[S6]}$$

where ele is the elevation referenced to the WGS84 ellipsoid, $geoid$ is the geoid, and MDT is the local ocean mean dynamic topography. The EIGEN-6C2 gravitational model (22) is used to calculate Antarctic geoid (icgem.gfz-potsdam.de/ICGEM/).

The MDT near ice shelf fronts is calculated using ICESat GLAS data coverage over the six different oceans (28) in summer (from February to April) of Antarctica.

$$MDT = \frac{\sum_{i=1}^{n} \left(ele_{sea}(i) - geoid_{sea}(i) \right)}{n}, \qquad \text{[S7]}$$

where n is the number of points covering the specific oceans. More than a million GLAS points are used to calculate the MDTs in different ocean areas of Antarctica. The result shows that the MDTs range from −1.08 m to −1.24 m.

The FDC is used to account for the presence of a variable-density layer. The firn layer makes up the majority of the ice shelf thickness uncertainty, and the FDC can dominate the error budget in the ice thickness estimates from surface elevation, assuming hydrostatic equilibrium (8, 27). It therefore complicates an accurate assessment of the ice shelf mass balance, because the

greatest uncertainty arises in the calculation of the influx across the GL and mass gain or loss from ice front advance and retreat.

The FDC can be estimated by a firn densification model or by combining the thickness and elevation measurements.

We use recently updated Antarctic FDC from a recent firn densification model (FDM) (29). The FDM was forced at the surface by the surface mass balance, surface temperature, and near-surface wind speed from a regional atmospheric climate model RACMO2/ANT, which was, in turn, forced at its lateral boundaries with a global atmospheric reanalysis from 1979, continuously updated in real time (ERA-Interim) reanalysis data. Then, the FDC parameter was modeled from RACMO2/ANT model data available for the period 1979–2009 at a temporal resolution of 6 h and a spatial resolution of 27 km. Liquid water processes (meltwater percolation, retention, and refreezing) are also included (29). However, the effect of heterogeneous infiltration and refreezing has not been investigated at any level (e.g., ref. 30).

Although the depth and density of the firn layer cannot be detected by satellite, FDC can be calculated from the true thickness and freeboard of the ice shelf by combining Eqs. S4 and S5.

$$\Delta h = \frac{\rho_w}{\rho_i} h_{asl} - \frac{(\rho_w - \rho_i)}{\rho_i} H. \qquad \text{[S8]}$$

Crossover points between MCORDS and GLAS tracks are used to estimate the firn correction. Because of the limited number of crossover points, the results are only used to determine the modeled FDC uncertainty.

The RACMO model has limitations in estimating FDC because of complex heterogeneous infiltration and refreezing for situations where surface melt is significant (30). To weaken this limitation, we correct the FDC in blue ice and melting areas using a land cover map. The Antarctic land cover map was drawn by the College of Global Change and Earth System Science at Beijing Normal University. A classification system of Antarctic land cover was established with six categories and conducted by combining computer-based and manual interpretation methods based on an improved Landsat Image Mosaic of Antarctica (31). It was produced with the combined use of 1,073 scenes of Landsat-7 ETM+ obtained during 1999–2003 and MODIS data acquired in 2005 covering from 82.5°S latitude to South Pole at 90°. The areas of each category of blue ice, crevasse, ice-free rock, water body, moraine, and firn are: 225,207 km^2 (1.65%), 7,153 km^2 (0.05%), 72,958 km^2 (0.535%), 189 km^2 (0.001%), 310 km^2 (0.003%), and 13,337,393 km^2 (97.7%), respectively. This land cover map was used to correct values of FDC to 0 for areas of blue ice and water body in this paper. In individual thickness calculation, the FDC of the GLAS or MCORDS measurement locations within 1 km of blue ice or melt pond is set to zero.

GL thicknesses. The GL positions come from combined MEaSUREs (20) and ASAID GL (21), just as it is used in delineation of ice shelf extent. The GL location precision is very important, because inferred grounded ice thickness may be erroneously high if we incorrectly assume hydrostatic equilibrium. Most GL positions use the MEaSUREs GL, which is thought to be more systematic and precise (8, 10). To minimize the risk of including the measurements of grounded ice and ice shelf ice far away from the GL, only the measurements within a distance of 900 m from the GL are used. First, the vector GL map is converted to raster GL at 900 m resolution, which is equal to the pixel size of the velocity data, and then converted to point vector GLs. Second, the GL points with measurements within a distance of 450 m are selected. Measurements of a GL thickness that fall beyond 3 SDs are excluded, and the mean of the rest is taken as the thickness of this GL point. Then, the remaining GL points with measurements within a distance of 450 m are selected.

Their thicknesses are determined as above. Finally, the thickness of the other GL points is determined from these points through the shortest-distance principle.

Subbasin average thickness of ice front change area. Considering the low-density distribution of both GLAS points and MCORDS points in the change areas (including advance, retreat, and iceberg calving) at the ice front, we use the mean value of all individual measurements covering the ice front change area (excluding the measurements that fall beyond 3 SDs) in a subbasin system as the thickness in mass estimation of advance, retreat, and iceberg calving in this subbasin system (Dataset S1).

Ice flow velocity. We use MEaSUREs Interferometry Synthetic Aperture Radar (InSAR)-based velocity data (19) at a resolution of 900 m for the period 2007–2008 derived from six sensors (available at nsidc.org/data/docs/measures/nsidc0484_rignot). The total error (the square root of the sum of the independent errors squared) of MEaSUREs velocity ranges from 1 m/y to greater than 17 m/y (the average is 4 m/y), and average direction error is 1.7° (8). MEaSUREs velocity is used in flow-line tracking (*Antarctic surface flow-line mapping*) and GL flux calculation (*Cross-GL fluxes*).

Ice shelf advance or retreat. We obtained Antarctic ice shelf extents in August 2005 and August 2011 from ASAR mosaic images combined with the GL and island area. The advance or retreat area is calculated by spatial analysis using ArcGIS software. The change in the GL position is not included in this analysis. The two period data have a good spatial and temporal consistency. The geolocation accuracy between the two mosaic images is less than one pixel (75 m). The mean annual advance or retreat in 6 y instead of annual change is used to decrease the area detection error. Fig. 2 shows ice shelf advance or retreat between 2005 and 2011.

Ice shelf thickening or thinning. The mass gain or loss from ice shelf thickening or thinning is calculated by the area of floating parts and its average thickness change. We use the previous results of average ice shelf thickness change $\partial H/\partial t$ in ref. 13 derived using IceSat-1 GLAS data for the period 2003–2008 [available at www.nature.com/nature/journal/v484/n7395/full/nature10968.html#supplementary-information (Supplementary Table 1)]. There are some small ice shelves with no estimates. For these ice shelves, we use the measurements from adjacent shelves.

Cross-GL fluxes. Ice flux across the GL is determined using a new flow-line routing algorithm. To obtain detailed ice fluxes, the GL is divided into many small segments with identical length. A flux gate calculation is made for each line segment. The ice flux F_{Gi} across a line segment is calculated as

$$F_{Gi} = H_i V_i L_i \rho_i,\qquad\text{[S9]}$$

where V_i is magnitude of flow velocity, H_i is ice thickness, and the across-flow width of the flux gate, L_i, is calculated as

$$L_i = \Delta L \times \sin(\alpha),\qquad\text{[S10]}$$

where α is the angle between the ice flow direction and the line segment and ΔL is the pixel size of the velocity raster data (900 m).

A very important step in ice flux estimation is determining the overlap of the along-flow flux gates, which is likely to overestimate ice flux due to deviations of the GL. Based on flow-line routes, the overlap of the flux gates along the ice flow is considered and processed (Fig. S3). First, we track flow lines from the GL pixels (pixel size 900 m, same as the velocity raster data) that the middle points of the GL line segments fall in. Then we transform the vector flow-line map into a raster flow-line map with the same spatial resolution as the velocity data. The value of pixels covered by flow lines downstream of the GL is set to 1, and all other pixels are set to 0. We determine the overlap GL pixels. If every value of the four connected pixels of a GL pixel is 1, it is determined as an overlap GL pixel. Finally, redo steps 1 and 2 using the GL pixels without the overlaps at step 3 to examine whether there are

obvious missing pixels along a flow line in the new raster flow-line map compared with the one tracked from the original GL pixels. If there are, the pseudo-overlap GL pixels are detected and recovered. All of the GL line segments whose middle points fall in the true overlap GL pixel are determined as the overlap flux gates, which are excluded from the ice flux calculation.

SMB. The SMB (or surface accumulation and melt) are derived from the regional atmospheric climate model RACMO2/ANT for the period 1979–2009 at a temporal resolution of 6 h and a spatial resolution of 27 km (29) (provided by M. R. van den Broeke).

However, considering the consistence of temporal scale, the firn height change we used in this paper is derived from a firn model UUFIRNMODELv3.1/ANT forced by climate data from RACMOv3.2/ANT27 for the period 2003–2008 (13) (available at doi.pangaea.de/10.1594/PANGAEA.775983). They run for 99 sites on Antarctic ice shelves. Surface accumulation, melt, and mass balance of 99 sites were interpolated to all ice shelves using the shortest-distance principle. The volume mass is processed at 27-km spacing.

Iceberg calving. Iceberg calving detection is more than ice front change detection, because the ice front keeps flowing, i.e., ice front advance and iceberg calving occur at the same time. We detected the location of calving events, delineated the ice front, and then detected the calving area by ice front registration using the features on the ice shelf before and after calving (Fig. S4).

Calving events detection. Traversing Antarctic coastline and comparing with the ASAR WSM image mosaic in August of the current year (the original image) and the following year (the second image), calving events are detected according to the changes at the front of ice shelves. The ice shelf front is likely to calve when extending forward; if advance and retreat are equal, there may be no obvious change occurring to the ice shelf front. To avoid misjudgment caused by this, the ice front movements are estimated by flow-line methods. Thus, even if there is neither advance nor retreat occurring at the front of an ice shelf, calving could be detected. The calved area is an enclosed polygon between the outer boundary (ice shelf ice front) and the inner boundary (fracture line) over a year. The calved areas are manually detected by using coregistered pairs of consecutive August 2005, 2006, 2007, 2008, 2009, 2010, and 2011 Envisat ASAR image mosaics.

Recurrence interval. Recurrence interval is defined as the time between the two major calving events at the same calving front. Calving recurrence means that two calving events occur in the same spatial neighborhood and their areas are the same order of magnitude. In this paper, RADARSAT-1 mosaic images of 1997 and ASAR images from 2005 to 2011 can be used to determine recurrence frequency of calving events. Individual calved areas between 1997 and 2005 and calving events between 2005 and 2011 are first determined. If one calving event in this year is spatially adjacent to other calving events in another year between 2005 and 2011 and their calved areas are of the same order of magnitude, their recurrence interval is less than 7 y. If the remaining isolated calving events have the same spatial neighborhood with calved area between 1997 and 2011 and of the same size magnitude, their recurrence intervals is less than 14 y. The infrequent tabular iceberg calving process is marked by several decades of quiescence between major calving events. Thus, the recurrent calving events in our observation period of 1997–2011 can be seen as frequent calving events.

Iceberg calving C is calculated by annual cumulative calving area A_C and its mean subbasin ice thicknesses at ice front H_C (*Ice thicknesses*).

$$C = A_C H_C \rho_i.\qquad\text{[S11]}$$

Basal melt. The basal melt or freezing is estimated at subbasin scale from the results of ice shelf mass balance, estimated from ice shelf thickness and extent change, ice flux at GL, SMB, and iceberg

calving. These data do not have exact time consistency. Ice shelf net thickening and SMB are averages for the period 2003–2008, ice flux is the average for 2007–2008, and iceberg calving is the average for 2005–2011. Thus, we see basal melt calculated in this study as an estimate for the average of period 2003–2011. The basal melt in 2003–2011 is given both in mass per year (gigatonnes per year) and in ice equivalent thickness (assuming a density of 917 kg/m^3) per year (meters per year) (Dataset S1).

Uncertainty Estimation. The uncertainty assessment is done separately for each subbasin. We assume the subbasins have dependencies in a sector but the sectors are independent of each other. The uncertainty estimation follows the rules of error propagation.
Density uncertainties. The uncertainties of both ρ_i and ρ_w are around 5 kg/m^3 (27).
Area uncertainties. Area error is smaller than other errors. The uncertainty is determined by the geolocation accuracy of the GL (100 m) (10) and delineated boundary at ice shelf front or boundary of calving area. The standard uncertainty of area is given as

$$u_A = 0.05 \times l, \qquad \textbf{[S12]}$$

where l is the perimeter (kilometers) of the area A (square kilometers). Eq. **S12** is justified based on the comparison between the same area delineated from ASAR image at 75-m spacing and that from RADARSAT image at 25-m spacing.
Thickness uncertainties.
  Uncertainty of individual MCORDS thickness. Uncertainty of individual MCORDS thickness includes systematical and random standard uncertainty u_{Hs}, u_{Hr},

$$u_H = \sqrt{u_{Hs}^2 + u_{Hr}^2}. \qquad \textbf{[S13]}$$

The systematical error mainly comes from instruments. The data are not radiometrically calibrated. The primary error of ice penetrating radar data consists of system electronic noise, multiple reflectors, and off-nadir reflections. No compensation was done for a firn layer by MCORDS SAR processing where the ice is treated as a homogeneous medium with a dielectric of 3.15 and the dielectric error is expected to be on the order of 1% for typical dry ice (26). The dielectric error is given by

$$u_{Hr} = \frac{H}{2} \varepsilon_{\%error} = 0.005 \times H. \qquad \textbf{[S14]}$$

Crossover analysis is used for the estimate of MCORDS ice thickness random error. For MCORDS L2 Ice Thickness, the crossover errors measurements are available from the 2009 Operation IceBridge campaign, and are provided by the Center for Remote Sensing of Ice Sheets (CReSIS). They are the only reliable estimate of thickness measurement errors available, but these crossover errors have not yet covered all of the Antarctic campaigns or data covering areas. The MCORDS L2 Ice Thickness data sets of Antarctic campaigns from 2009 to 2011 are used in this study. The CReSIS's crossover error analysis method is used here. The process is as follows. (*i*) Calculate crossover points and difference distribution. (*ii*) Discard extreme values in locations where thickness is 0 or very small, and the terrain has dramatic ups and downs, such as in mountainous areas. First, only thickness data with high quality of 1 (high confidence pick) are chosen. Second, for the areas where thickness is larger than 4 m, the triple standard difference method (3-δ principle) is used repeatedly to filter these extreme values until the change of SD is less than 1 m. (*iii*) Determine measurement error (error estimation).
The result of u_{Hr} is 23.6 m, which is estimated from 14,322 crossover points, thus,

$$u_{H_{i\_IB}} = \sqrt{23.6^2 + (0.005 \times H)^2}. \qquad \textbf{[S15]}$$

Uncertainty of estimated FDC. The uncertainty of individual estimated FDC from MCORDS thickness and GLAS freeboard is calculated as

$$u_{\Delta h} = \sqrt{\left(\frac{\rho_w}{\rho_i}\right)^2 u_{h_{asl}}^2 + \left(\frac{\rho_w - \rho_i}{\rho_i}\right)^2 u_H^2}, \qquad \textbf{[S16]}$$

where $u_{h_{asl}}$ is uncertainty of GLAS freeboard, as discussed in Eq. **S21**.
The modeled FDC have a good agreement with the ice core measurements data (29), but the in situ measurements are limited. There is no available error estimation of modeled FDC. We used 105 grids of modeled FDC, each of which contains more than 30 estimated FDC points (more than 3,150 crossover points between GLAS and MCORDS), to estimate the uncertainty of the modeled FDC. The standard uncertainty of the average estimated FDC of a grid is calculated as

$$u_{\Delta h_{ge}} = \sqrt{\frac{u_{\Delta h}^2 + \sigma_{\Delta h_{ge}}^2}{n}}, \qquad \textbf{[S17]}$$

where Δh_{ge} is the average estimated FDC of a grid, Δh is an individual estimated FDC, and n is the number of samples in a grid. The mean of the individual standard uncertainty of the grid average estimated FDC is 0.57 m, ranging from 0.286 m to 1.17 m.
If the estimated grid average FDC is thought of as true value, the standard uncertainty of modeled FDC is calculated as follows.

$$u_{\Delta h_{gm}} = \sqrt{\frac{\sum_{i=1}^{n} \left(\Delta h_{gm} - \Delta h_{ge}\right)^2}{N-1}}, \qquad \textbf{[S18]}$$

where Δh_{gm} is the individual modeled FDC, and N is the number of sample grids; 105 sample grids are used to estimate the standard uncertainty. The result showed that the standard uncertainty is 3.04 m. If we use a linear LSE to correct the modeled FDC, the standard uncertainty of the corrected modeled FDC is 2.88 m. In fact, the estimated grid average FDC also has its errors.
Uncertainty of individual equivalent thickness estimated from MCORDS thickness. The uncertainty of individual MCORDS equivalent thickness is determined by uncertainties of MCORDS thickness u_H and FDC $u_{\Delta h}$. The combined standard uncertainty of an individual estimation is given as

$$u_{H_{i\_IB}} = \sqrt{u_H^2 + u_{\Delta h}^2} = \sqrt{23.7^2 + (0.005 \times H)^2}. \qquad \textbf{[S19]}$$

The result showed that the MCORDS ice equivalent thickness error is dominated by MCORDS thickness measurement.
Uncertainty of individual equivalent thickness estimated from GLAS thickness. Crossover analysis between GLAS and MCORDS thicknesses is also used to estimate the uncertainty of GLAS ice thickness. The uncertainty of GLAS thickness estimated is 29.3 m from 623 crossover point pairs.
The uncertainty of GLAS ice thickness is also estimated from uncertainties of estimated freeboard $u_{h_{asl}}$ and modeled FDC $u_{\Delta h}$.
Ignoring the uncertainty of density of ρ_w and ρ_i, the uncertainty of GLAS ice thickness can be estimated as

$$u_{H_{i\_GS}} = \frac{\rho_w}{\rho_w - \rho_{ice}} \sqrt{u_{h_{asl}}^2 + u_{\Delta h}^2}. \qquad \text{[S20]}$$

The uncertainty of ice shelf freeboard is mainly caused by GLAS elevation measurement, the geoid correction, and the local mean dynamic topography correction. *MDT* is calculated from ele_{sea} and $geoid_{sea}$ in the local ocean near ice shelf fronts, so it probably has little correlation with *ele* and *geoid* of the ice shelf. The three error parts are likely to be independent of each other. The combined standard uncertainty of ice shelf freeboard measurement can be represented as

$$u_{h_{asl}} = \sqrt{u_{ele}^2 + u_{geoid}^2 + u_{MDT}^2}, \qquad \text{[S21]}$$

where u_{ele}, u_{geoid}, and u_{MDT} are standard uncertainty of *ele*, *geoid*, and *MDT*, respectively.

The GLAS single-shot error sources for elevation measurements are mainly from precision orbit determination, precision attitude determination, and atmospheric delay (16). Additional error sources arise on the ice shelves from the tide model the inverse barometer correction and variation from mean dynamic topography. The combined individual elevation uncertainty is estimated as 0.147 m.

The comparison of geoid heights derived from the EIGEN-6C2 model with GPS/leveling derived geoid values from United States, Canada, Europe, Australia, and Japan [Spectral Comparison with the Model EIGEN-6C2 (icdc.zmaw.de/geoid_eigen.html?&L=1)]. It gave a root-mean-square difference of up to 0.249 m and a total error budget of 0.216 m. There is no direct comparison from Antarctica, and we gave Antarctic EIGEN 6C-2 geoid standard uncertainty of 0.249 m.

The standard uncertainty contributions of mean dynamic topography are from GLAS elevation measurement, geoid measurement, and its spatial variation. The spatial averaging over the seven ocean areas near Antarctic coast employs between 148,000 and 400,000 points. The uncertainty in individual elevation measurements along an ICESat pass is thought to be correlated, but elevation measurements between ICESat passes are probably independent (13). We assumed the geoid uncertainty is spatially independent. The combined uncertainty of averaged mean dynamic topography can be calculated as

$$u_{MDT} = \sqrt{u_{ele}^2 \left(\frac{1}{n_{passes}} - \frac{1}{n_{points}} \right) + \frac{u_{geoid}^2}{n_{points}} + \frac{\sigma_{MDT}^2}{n_{points}}}, \qquad \text{[S22]}$$

where σ_{MDT} is the SD of averaged mean dynamic topography and n_{points} and n_{passes} are the number of elevation measurements and the number of unique combinations of ICESat passes, respectively. The combined standard uncertainty u_{MDT} is up to 0.008 m.

Combining these three uncertainties gives an individual uncertainty of ice shelf freeboard of 0.289 m as follows.

$$u_{h_{asl}} = \sqrt{u_{\overline{X}_{ele}}^2 + u_{\overline{X}_{geoid}}^2 + u_{h_{sea}}^2} = 0.289. \qquad \text{[S23]}$$

Thus, combining the uncertainties of freeboard and FDC gives an individual uncertainty of GLAS ice thickness as follows.

$$u_{H_{i\_GS}} = \frac{1,027}{1,027 - 917} \sqrt{0.289^2 + 2.42^2} = 23.4. \qquad \text{[S24]}$$

The uncertainty of subbasin average ice thickness of change and calving area at ice shelf front $u_{\overline{H}}$. Considering the low density of both GLAS points and MCORDS points in the changed area at the ice front,

we take the subbasin average ice thickness as the ice thickness of the changed area. Since the measurement errors of MCORDS ice thickness and GLAS ice thickness are in a similar range, both MCORDS and GLAS are used in this estimation. Thus,

$$u_{\overline{H}} = \sqrt{\frac{n_{IG}}{n} u_{H_{i\_IS}}^2 + \frac{n_{GS}}{n} u_{H_{i\_GS}}^2 + \frac{\sigma_{\overline{H}}^2}{n}} \qquad \text{[S25]}$$

where n_{IG}, n_{GS}, and n are the number of MCORDS, GLAS, and total measurements used; $\sigma_{\overline{H}}$ is the SD of the total thickness measurements.

The uncertainty of ice thickness at the GL $u_{H_{i\_MO}}$. The ice thicknesses of uniform discrete units of 900 m in size at the GL are directly or indirectly determined by MCORDS ice thickness and GLAS ice thickness. The units with no GLAS or MCORDS thicknesses are interpolated by those nearby. The uncertainty of ice thickness $u_{H_{i\_MO}}$ is given as

$$u_{H_i} = \begin{cases} u_{H_{i\_IB}} \\ u_{H_{i\_GS}} \\ u_{H_{i\_MO}} \end{cases} . \qquad \text{[S26]}$$

The error of interpolated ice thicknesses is given as 100 m (10).

$$u_{H_{i\_MO}} = 100. \qquad \text{[S27]}$$

Thickness change uncertainties.

Uncertainty estimation of $u_{\Delta H}$. The data of ΔH estimated from GLAS elevation change are from Pritchard et al. (13), and their overall combined uncertainty $u_{\Delta H}$ is dominated by the uncertainty in the FDC. We derived the uncertainty estimation of $u_{\Delta H}$ from their elevation change Δh_{ele} uncertainty estimation $u_{\Delta h_{ele}}$,

$$u_{\frac{\Delta H}{\Delta T}} = \frac{1,027}{1,027 - 917} \times u_{\frac{\Delta h_{ele}}{\Delta T}}. \qquad \text{[S28]}$$

The data are nearly ice shelf independent, and the uncertainty ranged from 0.03 to ~0.50 m. There are still missing data in some areas where we used the proximity principle to estimate ΔH, and gave them the maximum error of 0.50 m.

Uncertainty estimation of $u_{\Delta H_{Accu}}$, $u_{\Delta H_{Melt}}$. The values of ΔH_{Melt} and ΔH_{Accu} are estimated by combining the results of the firn model UUFIRNMODELv3.1/ANT forced by climate data from RACMOv3.2/ANT27 and elevation change obtained from ICESAT GLAS data from 2003 to 2008. An estimated uncertainty in the long-term accumulation trend of 8% is based on the strong relationship between accumulation and temperature found in RACMO2, whereas an uncertainty in RACMO2 surface melt rate at 20% is estimated by comparing with observed melt rates at two sites (13).

The data are nearly ice shelf independent. The ArcGIS shapefile of ice shelf extent are transformed onto a 27 km × 27 km grid cell. The cell accumulation and melt are obtained from the original point data by using the proximity principle. The long-term annual average accumulation and melt products of the firn model UUFIRNMODELv3.1/ANT are used in the missing data areas. Because the accumulation is much larger than surface melt, the uncertainties of SMB are dominated by the uncertainties of mean annual accumulation.

Velocity Uncertainty at the GL. The total velocity error (the square root of the sum of the independent errors squared) of Antarctica ranges from 1 m/y to greater than 17 m/y. We take the average uncertainty of velocity at the GL to be 4 m/y (8).

1. Joughin I, MacAyeal DR (2005) Calving of large tabular icebergs from ice shelf rift systems. *Geophys Res Lett* 32(2):L02501.
2. Fricker HA, Young NW, Allison I, Coleman R (2002) Iceberg calving from the Amery ice shelf, East Antarctica. *Ann Glaciol* 34(1):241–246.
3. Bassis JN, Jacobs SS (2013) Diverse calving patterns linked to glacier geometry. *Nat Geosci* 6(10):833–836.
4. Bassis JN, Fricker HA, Coleman R, Minster J-B (2008) An investigation into the forces that drive ice-shelf rift propagation on the Amery Ice Shelf, East Antarctica. *J Glaciol* 54(184):17–27.
5. Scambos TA, Hulbe CL, Fahnestock MA (2003) Climate-induced ice shelf disintegration in the Antarctic Peninsula. *Antarct Res Ser* 79:79–92.
6. Scambos TA, et al. (2009) Ice shelf disintegration by plate bending and hydro-fracture: Satellite observations and model results of the 2008 Wilkins ice shelf break-ups. *Earth Planet Sci Lett* 280(1):51–60.
7. MacAyeal DR, Scambos TA, Hulbe CL, Fahnestock MA (2003) Catastrophic ice-shelf break-up by an ice-shelf-fragment-capsize mechanism. *J Glaciol* 49(164):22–36.
8. Rignot E, Jacobs S, Mouginot J, Scheuchl B (2013) Ice-shelf melting around Antarctica. *Science* 341(6143):266–270.
9. York D, Evensen NM, Martınez ML, Delgado JDB (2004) Unified equations for the slope, intercept, and standard errors of the best straight line. *Am J Phys* 72(3):367–375.
10. Rignot E, et al. (2008) Recent Antarctic ice mass loss from radar interferometry and regional climate modelling. *Nat Geosci* 1(2):106–110.
11. Timmermann R, Wang Q, Hellmer HH (2012) Ice shelf basal melting in a global finite-element sea ice/ice shelf/ocean model. *Ann Glaciol* 53(60):303–314.
12. Hellmer HH (2004) Impact of Antarctic ice shelf basal melting on sea ice and deep ocean properties. *Geophys Res Lett* 31(10):L10307.
13. Pritchard HD, et al. (2012) Antarctic ice-sheet loss driven by basal melting of ice shelves. *Nature* 484(7395):502–505.
14. Jezek K, Farness K, Carande R, Wu X, Labelle-Hamer N (2003) RADARSAT 1 synthetic aperture radar observations of Antarctica: Modified Antarctic Mapping Mission, 2000. *Radio Sci* 38(4):8067.
15. Scambos TA, Haran TM, Fahnestock MA, Painter TH, Bohlander J (2007) MODIS-based Mosaic of Antarctica (MOA) data sets: Continent-wide surface morphology and snow grain size. *Remote Sens Environ* 111(2):242–257.
16. Zwally HJ, et al. (2002) ICESat's laser measurements of polar ice, atmosphere, ocean, and land. *J Geod* 34(3):405–445.
17. Allen C, et al. (2012) Antarctic ice depthsounding radar instrumentation for the NASA DC-8. *IEEE Trans Aerosp Electr Syst* 27(3):4–20.
18. Fretwell P, et al. (2013) Bedmap2: Improved ice bed, surface and thickness datasets for Antarctica. *Cryosphere* 7(1):375–393.
19. Rignot E, Mouginot J, Scheuchl B (2011) Ice flow of the Antarctic ice sheet. *Science* 333(6048):1427–1430.
20. Rignot E, Mouginot J, Scheuchl B (2011) Antarctic grounding line mapping from differential satellite radar interferometry. *Geophys Res Lett* 38(10):L10504.
21. Bindschadler R, et al. (2011) Getting around Antarctica: New high-resolution mappings of the grounded and freely-floating boundaries of the Antarctic ice sheet created for the International Polar Year. *Cryosphere* 5(3):569–588.
22. Förste C, et al. (2011) EIGEN-6–A new combined global gravity field model including GOCE data from the collaboration of GFZ-Potsdam and GRGS-Toulouse. *Geophys Res Abstr* 13: EGU2011-3242-2.
23. Jezek KC (1999) Glaciological properties of the Antarctic ice sheet from RADARSAT-1 synthetic aperture radar imagery. *Ann Glaciol* 29(1):286–290.
24. Shepherd A, et al. (2012) A reconciled estimate of ice-sheet mass balance. *Science* 338(6111):1183–1189.
25. Liu H, Jezek KC (2004) A complete high-resolution coastline of Antarctica extracted from orthorectified Radarsat SAR imagery. *Photogramm Eng Remote Sensing* 70(5):605–616.
26. Fujita S, et al. (1999) Nature of radio echo layering in the Antarctic Ice Sheet detected by a two-frequency experiment. *J Geophys Res* 104(B6):13013–13024.
27. Griggs JA, Bamber JL (2011) Antarctic ice-shelf thickness from satellite radar altimetry. *J Glaciol* 57(203):485–498.
28. Kurtz NT, Markus T (2012) Satellite observations of Antarctic sea ice thickness and volume. *J Geophys Res* 117(C8):C08025.
29. Ligtenberg SRM, Helsen MM, van den Broeke MR (2011) An improved semi-empirical model for the densification of Antarctic firn. *Cryosphere* 5:809–819.
30. Harper J, Humphrey N, Pfeffer WT, Brown J, Fettweis X (2012) Greenland ice-sheet contribution to sea-level rise buffered by meltwater storage in firn. *Nature* 491(7423):240–243.
31. Hui F, et al. (2013) An improved Landsat Image Mosaic of Antarctica. *Sci China Earth Sci* 56(1):1–12.
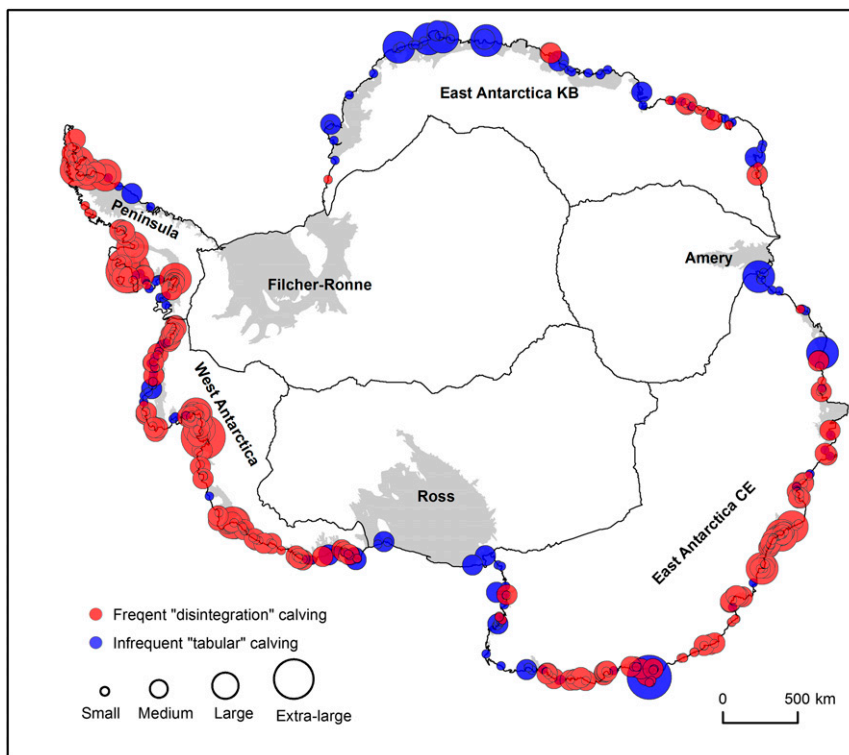
Fig. S1. Spatial distribution of Antarctic calving events in different calving styles and calving scales from 2005 to 2011. Four calving scales are divided: small (1~10 km²), medium (10~100 km²), large (100~1,000 km²) and extra-large (larger than 1,000 km²).

Fig. S2. Antarctic flow-line map. Different colors identify different basin flow systems.

Fig. S3. Flux gate filtering. The background image is MOA. (*A*) Tracking flow lines from GLs: The yellow line marks the GLs, the black boxes are the GL pixels, and the gray lines are flow lines tracking from the GL pixels. (*B*) Determining overlapping GL pixels: The red pixels are flow lines covering pixels and the green boxes are overlapping GL pixels along the flow. (*C*) Examining mistakenly deleted GL pixels: The red pixels are flow line covering pixels excluding the overlapping GL pixels in *B* and blue boxes are pseudo-overlapping GL pixels.
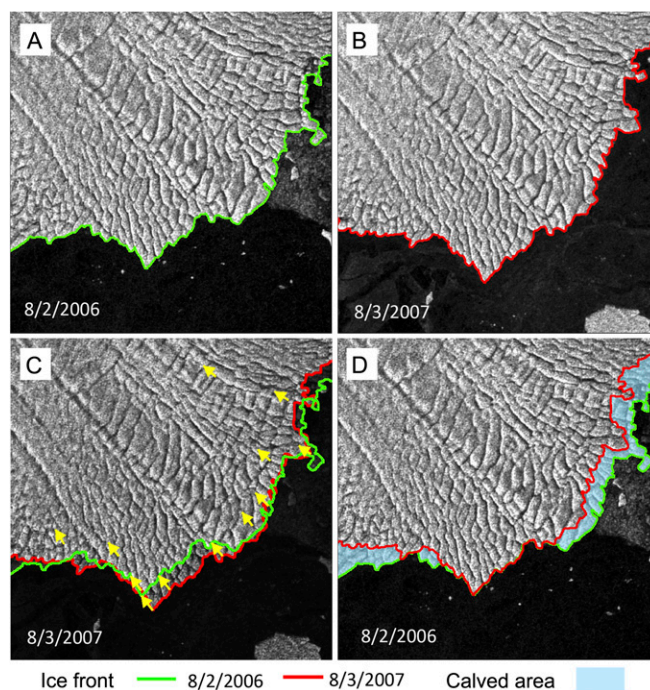
Fig. S4. Sketch map of calving area detection on ASAR WSM images: (*A* and *B*) ice front lineated from ASAR images; (*C*) ice front registration by feature tracking; and (*D*) the ice front spatially shifted according to ice front registration and calving areas detected.

Table S1. Comparison of the ice front flux calculated in this study (averaged over 2005–2011) and Rignot et al. (8) (averaged over 2007–2008)

Sector	This study, Gt/y	Rignot, Gt/y
Antarctica	1025 ± 39	1089 ± 139
Filchner-Ronne	212 ± 17	221 ± 26
East Antarctica KB	119 ± 17	130 ± 22
Amery	35 ± 2	50 ± 8
East Antarctica CE	270 ± 15	236 ± 33
Ross	148 ± 6	146 ± 12
West Antarctica	197 ± 17	225 ± 17
Peninsula	44 ± 19	69 ± 13

Table S2. Area mean melt rate (meter ice equivalent per year, assuming density is 917 kg/m^3) of the larger Antarctic ice shelves

Locations	This study	Glaciological estimate	FESOM	BRIOS
Antarctica	1.07	1.05	1.16	0.80
Sum of ten	0.50	0.58	0.98	0.79
Filchner-Ronne	0.02	0.38	0.34	0.32
Brunt + Riiser-Larsen	0.27	0.13	0.92	3.38
Fimbulisen +Jelbart	0.77	0.40	2.80	4.91
Larsen C	1.04	0.49	1.00	0.60
George VI	4.02	4.14	3.60	0.43
Abbot	1.17	1.90	3.10	0.60
Pine Island	14.00	17.66	3.10	—
Getz	4.82	4.65	5.40	1.95
Ross	0.06	0.10	0.60	0.49
Amery	1.66	0.64	2.90	0.35

This study is averaged over 2003–2011. Glaciological estimate averaged over 2007–2008 (8), FESOM averaged over 1980–1999 (11), and BRIOS 2004 (12). "Sum of ten" refers to the 10 largest ice shelves alone. —, no data.

Table S3. The spatial distribution of total calving events of the infrequent tabular calving and frequent disintegration calving in seven sectors (see Dataset S1) from 2005 to 2011

	Number of calving events		
Sector	Infrequent tabular calving	Frequent disintegration calving	All
Antarctica	152	427	579
Filchner-Ronne	0	0	0
East Antarctica KB	41	28	69
Amery	1	0	1
East Antarctica CE	45	177	222
Ross	5	0	5
West Antarctica	39	142	181
Peninsula	21	80	101

Table S4. Mean percentage of calving events, area, and mass loss for four different spatial scales from 2005 to 2011

	Frequency, %		Calving area, %		Mass loss, %	
Scale category	Annual mean	Range	Annual mean	Range	Annual mean	Range
Small (<10 km^2)	60.3 ± 0.1	[56.6,65.4]	5.9 ± 0.2	[3.5,13.4]	6.8 ± 0.1	[3.3,13.1]
Medium ($10-100$ km^2)	34.7 ± 0.3	[28.3,40.8]	26.5 ± 8.2	[9.2,79.7]	31.4 ± 7.8	[7.5,80]
Large ($100-1{,}000$ km^2)	4.5 ± 0	[1,7.2]	25.7 ± 7.6	[6.9,71.7]	24.5 ± 6.7	[4.5,68.1]
Extralarge ($>1{,}000$ km^2)	0.5 ± 0	[0,2.3]	41.8 ± 16.9	[0,78.1]	37.2 ± 15.9	[0,84.8]

Other Supporting Information Files

Dataset S1 (XLS)